ELSEVIER

Journal of Nuclear Materials 254 (1998) 158–174

journal of nuclear materials

Liquid immiscibility in a (O,U,Zr) model corium

C. Guéneau [a,*], V. Dauvois [a], P. Pérodeaud [b], C. Gonella [a], O. Dugne [b]

[a] *DCC / DPE / SPEA, CEA, CE Saclay, 91191 Gif-sur-Yvette cedex, France*
[b] *DCC / DTE / SIM, CEA Valrho, 26702 Pierrelatte, France*

Received 10 September 1997; accepted 23 December 1997

Abstract

New data on the miscibility gap in the liquid state in both O–U and O–U–Zr phase diagrams are reported. Mixtures are melted by electron bombardment. Tie-lines are determined in the O–U miscibility gap at 3090 K as well as in the O–U–Zr ternary system at 3223 K. 'Metallic' and 'oxide' liquids are immiscible in a large range of temperature and composition in both systems. The miscibility gap extent is extrapolated by thermodynamic calculations. The quenched microstructures of the different liquid phases are described and interpreted using a solidification path calculation. For the (O,U,Zr) alloys entering the miscibility gap, the minor oxide liquid phase is in the form of droplets in the metallic parent liquid. The droplets seem to segregate at the ingot surface. This leads to a layer formation in the case of the O–U system where there is the greatest difference between the two liquid compositions. © 1998 Elsevier Science B.V.

PACS: 64.75.+g; 81.20.Zx; 81.30.−t; 81.05.Je

1. Introduction

During a severe nuclear accident, the reactor assembly, mainly constituted of zircaloy sheaths and UO_2 fuel pellets, partially or wholly melts. The material resulting from the reactor melting, designated as corium, flows out at the bottom of the steel reactor vessel. Two outstanding scenarios are being studied (J.M. Seiler, private communication): (i) corium containment inside the reactor vessel whose external walls are cooled, (ii) the punching of the reactor vessel and spreading out of the corium on a refractory material core catcher [1]. To predict the heat transfer processes occurring in corium, the natures and relative fractions of solid and liquid phases must be known as a function of its composition and temperature. In both scenarios, the basic O–U–Zr phase diagram must be well known at high temperatures. A miscibility gap in the liquid state is found in a considerable number of metal–oxide systems such as Fe–O, and was also found in the O–U system [2]. The purpose of the present study is to determine the extent of the liquid miscibility gap in the O–U–Zr ternary system to better understand and then predict the presence and the possible segregation of the liquid phase at high temperatures in the corium. New experiments are undertaken to provide new data on the liquid miscibility gap in both O–U and O–U–Zr systems for use in thermodynamic calculations.

We first give the state-of-the-art O–U–Zr phase diagram and then describe the procedure for the alloy preparation. The results for the U–Cu reference system are first discussed. This system, which exhibits a large miscibility gap in the liquid state, was chosen as a reference case to test the efficiency of the experimental conditions for quenching the two liquid structures which have very different densities. Then, the experimental investigation of the miscibility gap in O–U and O–U–Zr is presented. Finally, the alloy microstructure is interpreted using a solidification path calculation performed with the Thermo-Calc software.

Thermo-Calc is a flexible software for all kinds of thermodynamic and phase diagram calculations. The evaluation of the thermodynamic properties of the phases are

* Corresponding author. DCC/DPE/SPEA, Bât. 125, CEA, CE Saclay, 91191 Gif-sur-Yvette Cedex, France. Tel.: +33-1 69 08 67 41; fax: +33-1 69 08 92 21; e-mail: cgueneau@cea.fr.

PII S0022-3115(98)00002-6

derived from an optimization procedure with the Parrot module developed by Jansson [3] contained in the Thermo-Calc databank system [4] by using all the available experimental phase diagram and thermodynamic data. The critical assessment of the O–U–Zr system and the associated thermodynamic database will soon be published in a next paper [5]. In the present work, phase diagram calculation is only used to discuss the consistency of the different experimental data and to interpret the quenched microstructure of the (O,U,Zr) melts.

2. State-of-the-art O–U–Zr system

The existence of a miscibility gap in the liquid state in the O–U binary system is the starting point of the miscibility gap in the O–U–Zr ternary diagram.

2.1. O–U system

The O–U phase diagram calculated with Thermo-Calc [5] is compared with the published experimental data [2,6–12] (J.J. Poupeau, private communication) in Fig. 1.

The UO_2-rich part of the diagram is accurately known. On the other hand, the experimental data for oxygen solubility in liquid uranium are not consistent. For example, at 2000°C, according to Edwards and Martin [2], the oxygen solubility limit in liquid uranium is very low, less than 1 at.%, while Guinet et al. [6] measured a much higher value of about 25 at.%. There is thus an uncertainty in the extent of the miscibility gap in the liquid state in which only liquid oxide composition is accurately known. The miscibility gap is very small according to Guinet et al. [6] and is very large for Edwards and Martin [2]. To calculate the phase diagram with Thermo-Calc, it is necessary to select the experimental data from the above references. Two arguments are considered to choose in a first step the data of Edwards and Martin. First, the high oxidation rate of native uranium can lead to an over-estimated value of the oxygen limit solubility. Second, in the O–U–Zr system, the miscibility gap in the liquid state has been experimentally displayed by Juenke and White [13] (Fig. 2) and Politis [14] (Fig. 3), respectively, along the UO_2–Zr and UO_2–$ZrO_{0.51}$ composition lines. All authors [13–16] report the presence of a large miscibility gap in this composition range except Hayward and George [17] who have not observed it in the UO_2–$ZrO_{0.54}$ section. In the first step, we assume that the miscibility gap exists along the UO_2–Zr and UO_2–$ZrO_{0.51}$. This means that the miscibility gap is very wide in the ternary starting from the O–U system. These data can only be consistent with a low oxygen solubility limit in liquid uranium. The data of Edwards and Martin are thus used in the calculation. It can be pointed out that the size of the miscibility gap as a function of temperature is not known.

2.2. O–U–Zr isothermal sections

The first investigations of the phase stability relations in the O–U–Zr system were carried out by Saller et al. [18], who proposed three tentative isothermal sections at temperatures up to 1100°C. Higher temperature isothermal sections were determined by Politis [14] and Hofmann et al. [15] at 1000, 1500 and 2000°C. Later, Skokan [16]

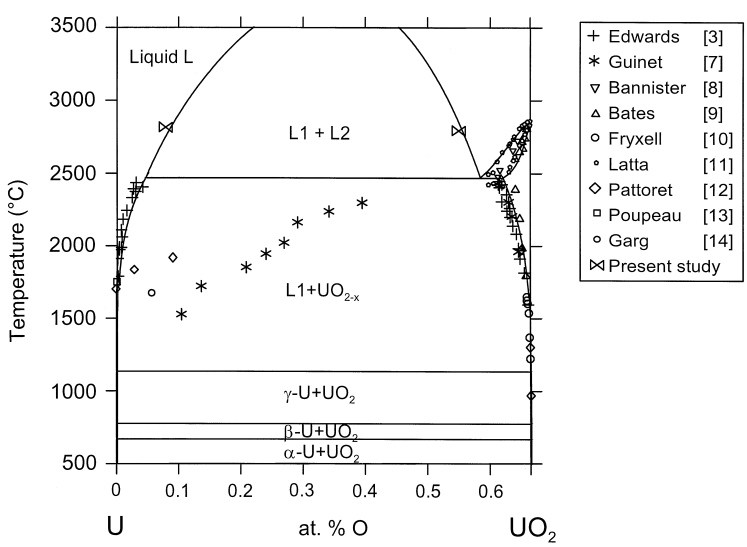

Fig. 1. Calculated U–UO_2 phase diagram. The tie-line experimentally determined at 3090 K is reported as well as the experimental results of the literature.

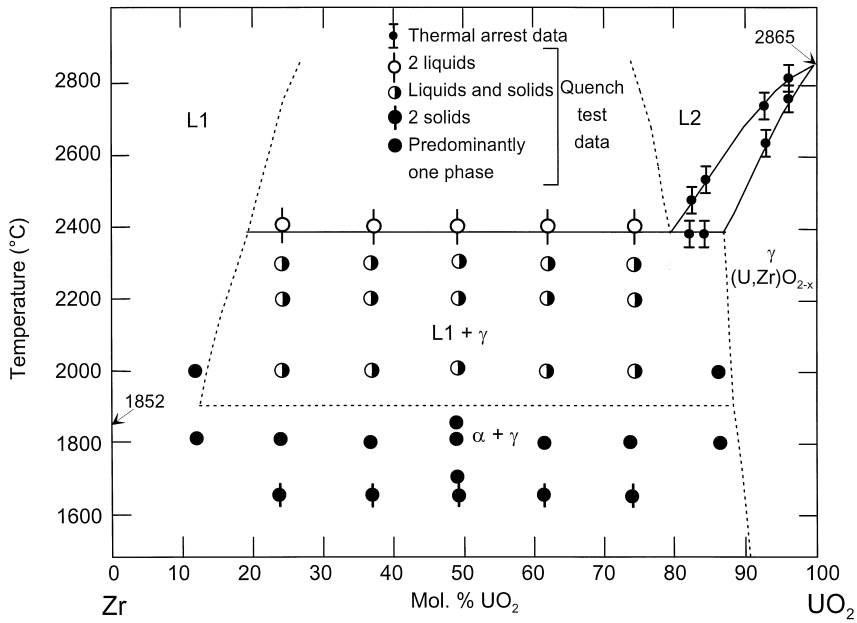

Fig. 2. Zr–UO_2 section according to Juenke and White [13].

extended the equilibria examinations between 1500 and 2000°C. Isothermal sections at 1000°C and 1400°C were experimentally investigated by Yamanaka et al. [19] and Miyake et al. [20].

Most of these experimental investigations concern the part of the diagram close to the UO_2–Zr composition line in order to study the interaction between the UO_2 fuel and the zircaloy. The uranium-rich corner is not well known. For example, at 2273 K, only the part close to the UO_2–Zr line composition was determined by Politis [14] (Fig. 3). The remaining part of the diagram was extrapolated. For this reason, in a previous study, a number of thermody-

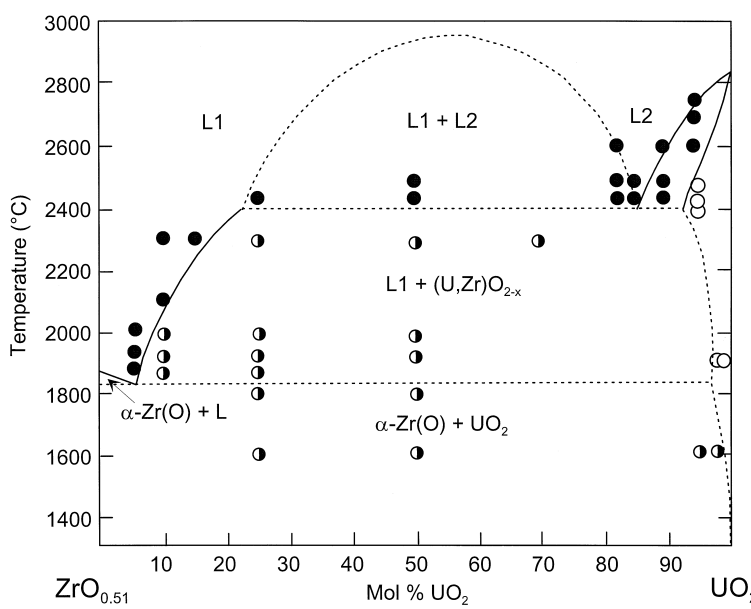

Fig. 3. $ZrO_{0.51}$–UO_2 section from Politis [14].

Table 1
Experimental conditions for the preparation of the uranium alloy by using electron bombardment heating

Alloy designation	Ingot initial overall composition (at.%)	Final overall alloy composition (at.%)	Surface melt temperature T_M (K)	Electron gun power (kW)	Power density (kW/cm^2)	Time at T_M (mn)	Ingot surface cooling time (s)	Melt thickness (mm)	Miscibility gap
U–Cu	29 Cu 71 U	27 Cu 73 U	not measured	6	0.49	3	40	17	observed
U–UO_2	46 O 54 U	not measured	3090 ± 100[a]	30	4.8	2	2–3	18	observed
UO_2–Zr (1)	48 O 26 Zr 26 U	42 O 43 Zr 15 U	not measured	8	0.242	15	12	4	not observed
UO_2–Zr (2)	48 O 26 Zr 26 U	35 O 54 Zr 11 U	not measured	20	0.81	11	not measured	13	not observed
U–ZrO_2 (1)	40 O 20 Zr 40 U	19 O 37 Zr 44 U	3223 ± 100[a]	40	10	2	4	11	observed
U–ZrO_2 (2)	40 O 20 Zr 40 U	48 O 41 Zr 11 U	3000 ± 100[a]	40	2.5	2	not measured	7	not observed
			2900 ± 100[b]						
U–ZrO_2 (3)	40 O 20 Zr 40 U	19 O 37 Zr 44 U	3150 ± 100[a]	40	10	2.25	not measured	11	observed

[a]Estimated from the evaporation model.
[b]Measured with a pyrometer.

namic properties of the O–U–Zr system were experimentally determined [21,22]; the [L/(U,Zr)O_{2-x}] liquidus position at 2273 K for U/Zr ~ 1.35, representative of the corium, was evaluated from the variation of the oxygen activity with the oxygen content. The oxygen activity was determined from measurements of the partial pressure of UO and U species by using high temperature mass spectrometry. The resulting value of 7 at.% differs from that estimated by Politis (about 20 at.%).

2.3. Composition / temperature vertical sections

At temperatures above 2000°C, phase equilibria are given on composition/temperature vertical sections for UO_2–Zr [13] (Fig. 2) and α-Zr(O)–UO_2 (Fig. 3) [14–17]. As reported above, all authors except Hayward and George [17] predict the presence of a large miscibility gap in the liquid state at temperatures above 2400°C. No experimental data outside the composition line close to Zr–UO_2 are available in the literature.

An overview of the earlier data shows some inconsistencies concerning the extent of the miscibility gap in the O–U binary as well as in the O–U–Zr system close to the UO_2–Zr and UO_2–α-Zr(O) composition lines.

The first calculation of the O–U–Zr phase diagram with Thermo-Calc by using the data of Edwards and Martin for the O–U binary leads to a wide miscibility gap in the ternary system. The two liquid phases exhibit very different compositions: one, metallic with a composition close to U–Zr; the other, oxygen-rich.

This large difference between the two liquid compositions could lead to a phase segregation phenomenon involving a change in the corium heat transfer processes during an accident. An experimental study has been thus undertaken to specify the extent of the miscibility gap in the ternary as a function of the temperature.

3. Experimental conditions

A preliminary study is made in reference to U–Cu system. Then experiments are undertaken with the O–U and O–U–Zr systems. The alloys are melted by electron bombardment at very high temperatures and then quenched. The experimental conditions for all the studied alloys are summarized in Table 1.

3.1. Materials

For the (U,Cu) alloy preparation, pure metallic uranium and Oxygen Free High Conductivity copper are used.

In the (U + UO_2) mixture, cylinders of UO_2 (SICN, 8-mm diameter and 10.5-mm height) are broken to 3-mm pieces. An ingot of pure natural uranium is placed above the UO_2 pieces.

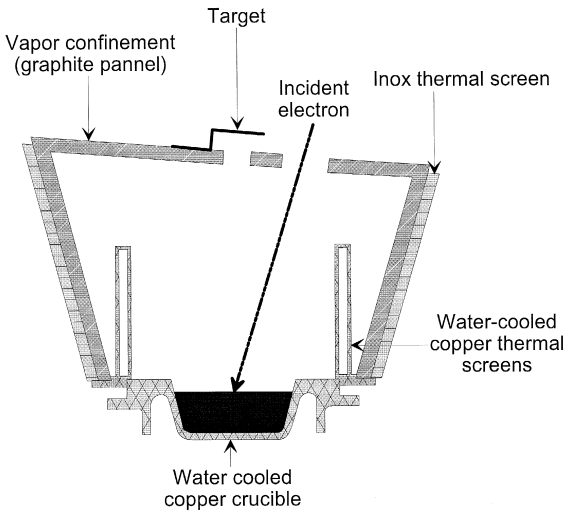

Fig. 4. Schematic view of the electron bombardment equipment.

Two preparation methods for the (O,U,Zr) ternary alloy are tested:

(i) (UO_2 + Zr) mixture in which 99.8 wt% purity zirconium (Puretech) is in the form of parallelepipeds (5 × 8 × 12 mm).

(ii) (U + ZrO_2) mixture with monoclinic crystalline structure zirconia pieces (3–12 mm) (99.7 wt% purity, CERAC).

3.2. Electron bombardment heating

An electron bombardment system is employed (Fig. 4).

Heating is provided by a 60-kW Leybold electron gun operating in a vessel where a secondary vacuum is maintained. The electron beam scans a rectangular surface of the ingot, whose size ranges between 2 cm × 2 cm and 6 cm × 5.5 cm, depending on the test. The ingot surface can be observed with a camera during the experiment. A 10-color pyrometer is used to measure the ingot surface temperature. The different mixtures are melted in a water-cooled copper axially symmetric crucible ($h = 45$ mm, $\phi \sim 110$ mm). The crucible temperature is controlled with thermocouples. The ingot is generally formed by performing several meltings at an intermediate power density to obtain a homogeneous and as large as possible melt zone without evaporating the constituents of the melt. The power density is quickly increased (in a few seconds) to reach the desired temperature for several minutes. The ingot is cooled by cutting off the electron beam. The cooling time of the ingot surface varies from 4 to 40 s depending on the test.

This type of heating temperatures of up to 3000°C to be reached. Furthermore, the use of a water cooled copper crucible prevents the chemical interaction between the alloy and its container. The disadvantage of the electron bombardment is the resulting temperature gradient between the ingot surface and bottom so that the liquid temperature is not homogeneous along the ingot thickness. The influence of the temperature gradient will be discussed for each test by considering the specimen homogeneity. Furthermore, the high temperature level and the focusing of the beam on a small surface area induce appreciable evaporation of the elements. It is then necessary to find a compromise by selecting the optimum heat flux, scanned surface, ingot thickness and time of heating. Because of evaporation, the alloy composition changes during the experiment. The final composition of the melt is measured by a post-mortem analysis of the ingot.

3.3. Melt temperature determination

The high temperature measurement is very difficult to perform. An evaporation model is used to estimate it and to help to define the experimental conditions.

3.3.1. Pyrometry

The measurement of the temperature at the melt surface is performed with a 10-wavelength pyrometer (0.5844 μm < λ < 1.033 μm). The high vaporization rate of the melt can induce a condensation at the surface of the window, behind which the optical measurement is done. This phenomenon can decrease the emitted signal then the temperature. A glass slide swept by an argon jet is thus placed ahead of the window. The measured temperature vs. time is given for the U–ZrO_2 (2) test in Fig. 5. The temperatures measured with the pyrometer are given with an estimated uncertainty of ±100 K.

3.3.2. Estimation by evaporation model (Appendix A)

The source flux F_S is measured by a simple weighing of the ingot and from the evaporation area and time. The source flux above the (O,U,Zr) melt is theoretically calculated as a function of the temperature by using a Langmuir flux for the U, UO, UO_2, UO_3, Zr, ZrO, ZrO_2 [11,23] (V. Dauvois, private communication) species (see Appendix A). The temperature of the melt is then deduced from the

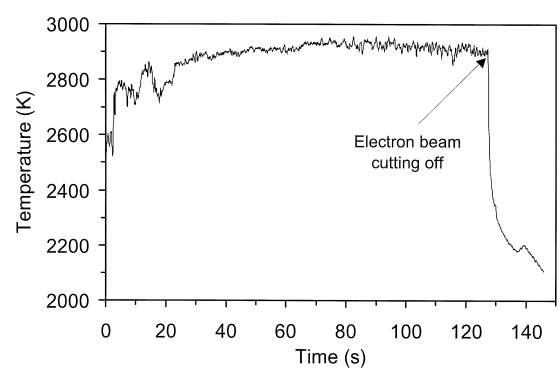

Fig. 5. Time dependence of the melt surface temperature measured with a 10-wavelength pyrometer for the U–ZrO_2 (2) test.

theoretical curve $F_S = f(T)$. The uncertainty on this temperature is estimated to be ± 100 K.

The melt temperatures determined by pyrometry and from the evaporation model are compared for the U–ZrO_2 (2) test (see Table 1). In view of the uncertainties of 100 K, it shows a correct agreement between both methods.

3.4. Microstructure analysis

For each test, a cross-section was cut from the ingot center. After polishing, the specimens were observed by using both optical and scanning electron microscopy (SEM). To accurately measure the element concentrations in the phases, particularly, the oxygen concentration, several techniques were used in order to obtain consistent results. The composition analysis was performed either with an electron dispersive spectrometry (EDS) or wavelength dispersive spectrometry (WDS). In addition to the phase composition measurement, it was necessary to determine the overall compositions of the melts. For these measurements, image analysis is used in addition to the above reported methods. As the temperature is estimated at the ingot surface, the overall composition analysis of the melts are performed close to the surface.

4. Experimental results

Initial experiments on the U–Cu system are carried out to test the specific conditions of heating where the melt is not isothermal, the convection is appreciable and the ingot cooling rate can be slow. It was also studied in order to have an idea of the morphology of the two liquid phases in case of a large difference in density. In the following discussion, L1 designates the U-rich liquid in all the systems and L2, the Cu-rich phase in U–Cu and the oxide-rich one in U–O and O–U–Zr.

4.1. Reference case: U–Cu system

The U–Cu phase diagram is given in Fig. 6 [24].

Initial observation of the ingot shows that the surface is enriched in copper. As only copper evaporated during the experiment ($p_{Cu} \sim 1000\ p_U$), a simple weighing of the ingot gives the final overall melt composition. A macroscopic view of the ingot section is shown in Fig. 7a. A thin upper layer enriched in copper, mainly constituted of UCu_5 can be observed (Fig. 7c). The remaining part of the ingot is enriched in uranium (Fig. 7d). The phase composition analysis is presented in Table 2. The overall composition of the ingot as well as those of the different areas are reported on the U–Cu phase diagram in Fig. 6. This clearly shows that the two layers correspond to the two liquid phases L1 and L2 whose compositions are in agreement with the phase diagram. The lighter liquid phase, enriched in copper, is segregated by gravitation at the surface of the melt. Some droplets of the copper-rich liquid phase are quenched during their rising to the surface (Fig. 7b).

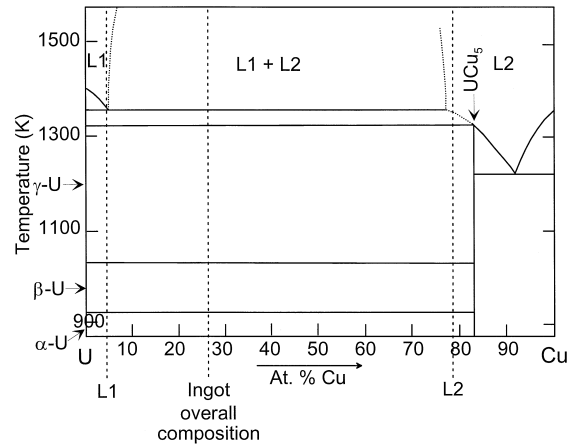

Fig. 6. U–Cu phase diagram according to Chiotti et al. [24] where the experimental compositions of the two liquids are reported.

This first experiment shows that the cooling rate of the melt is fast enough to quench the two liquid structures of the miscibility gap. Furthermore, the two liquid compositions are in agreement with those of the phase diagram. It also shows that under these experimental conditions, the two liquid phases clearly separate by gravitation to form two distinct layers in case of a large density difference.

4.2. O–U system

The estimated melt temperature at the ingot surface is 3090 ± 100 K. The vapour composition is 55 at.% O, corresponding to an enrichment in uranium of the melt during the test. An oxide-rich layer, of about 0.5 mm thickness, (Fig. 8a), not adhering to the rest of the ingot, is observed at the surface after solidification. A micrograph of the section under the surface layer is presented in Fig. 8b and shows the presence of droplets enriched in UO_2 in a U-enriched matrix. The droplets, located near the ingot surface, correspond clearly to the oxide liquid phase L2 of the miscibility gap. These spherical nodules cannot correspond to a solid phase which would be present during the experiment. In fact, at these composition and temperature, only liquid phases can be stable. Furthermore, these nodules cannot be formed during cooling as it would precipitate in the form of dendrites. The structure of the surface layer and of the droplet are very similar. It can be assumed that the oxide-rich liquid L2 rose to the melt surface due to its lower density. The microstructure of the oxide-rich liquid L2 is shown in Fig. 8c and d. During the miscibility gap crossing, some uranium-rich liquid L1 can be formed inside the droplet of oxide-rich liquid L2 and could correspond to the large area of uranium observed inside the droplet (Fig. 8c and d). Then, the oxide-rich liquid L2

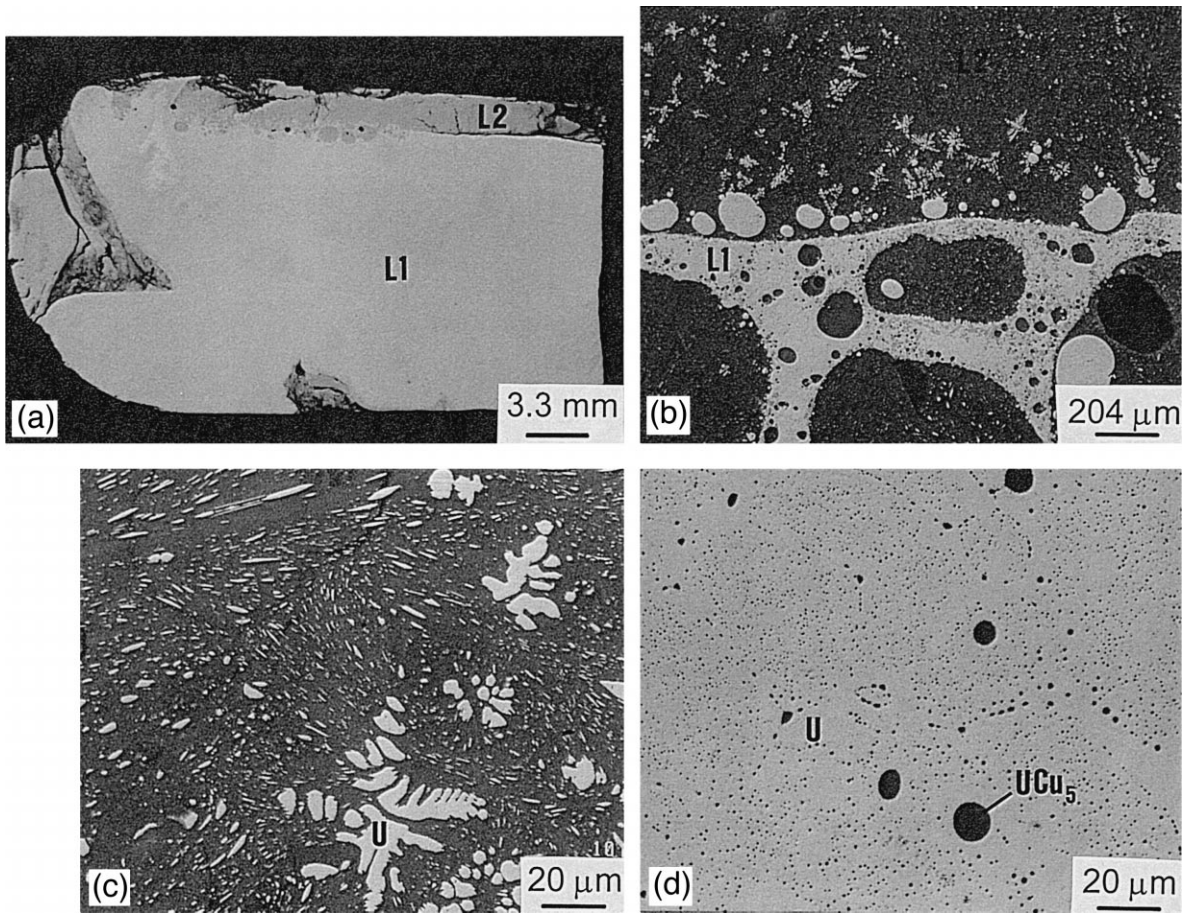

Fig. 7. (a) Ingot macroscopic view of the U–Cu test showing two layers corresponding to the two liquid phases L1 (U-rich) and L2 (Cu-rich) of the miscibility gap. (b) Electron micrograph showing the interface between the two layers in the U—Cu ingot. (c) Electron micrograph presenting the microstructure of the L2 copper-rich liquid phase of the U–Cu system. It consists of uranium dendrites in a UCu_5 matrix. (d) Electron micrograph presenting the microstructure of the L1 uranium-rich liquid phase of the U–Cu system. It consists of UCu_5 spherical precipitates in a U matrix.

decomposes into uranium dioxide and U-rich liquid L1 during the monotectic reaction [$L2 \rightarrow UO_{2-x} + L1$]. The monotectic structure could correspond to the small droplets of uranium in the oxide matrix. A small fraction of uranium dioxide should precipitate from the remaining U-rich liquid until the solidus temperature is reached. No uranium dioxide dendrites can be observed in the uranium-rich area. It can be assumed that the uranium dioxide grows by epitaxy from the solid formed at higher temperature. The parent uranium liquid L1 (Fig. 8e) follows the same solidification path but the relative phase fractions are not the same. During cooling, oxide-rich liquid L2 can appear in the form of droplets. Between the monotectic and the solidus temperature, uranium dioxide dendrites germinate

Table 2
Microstructure analysis of the U–Cu ingot

Overall composition of the liquid phases (at.%)	Phase	Phase composition (at.%)	
Copper-rich liquid (79 ± 1 Cu, 21 ± 1 U)	Uranium dendrites	0.8 ± 0.1 Cu	99.2 ± 1 U
	Rich copper matrix (two-phase)	81 ± 1 Cu	19 ± 1 U
Uranium-rich liquid (4 ± 1 Cu, 96 ± 1 U)	UCu_5 nodules	83 ± 1 Cu	17 ± 1 U
	Uranium matrix	0 Cu	100 U

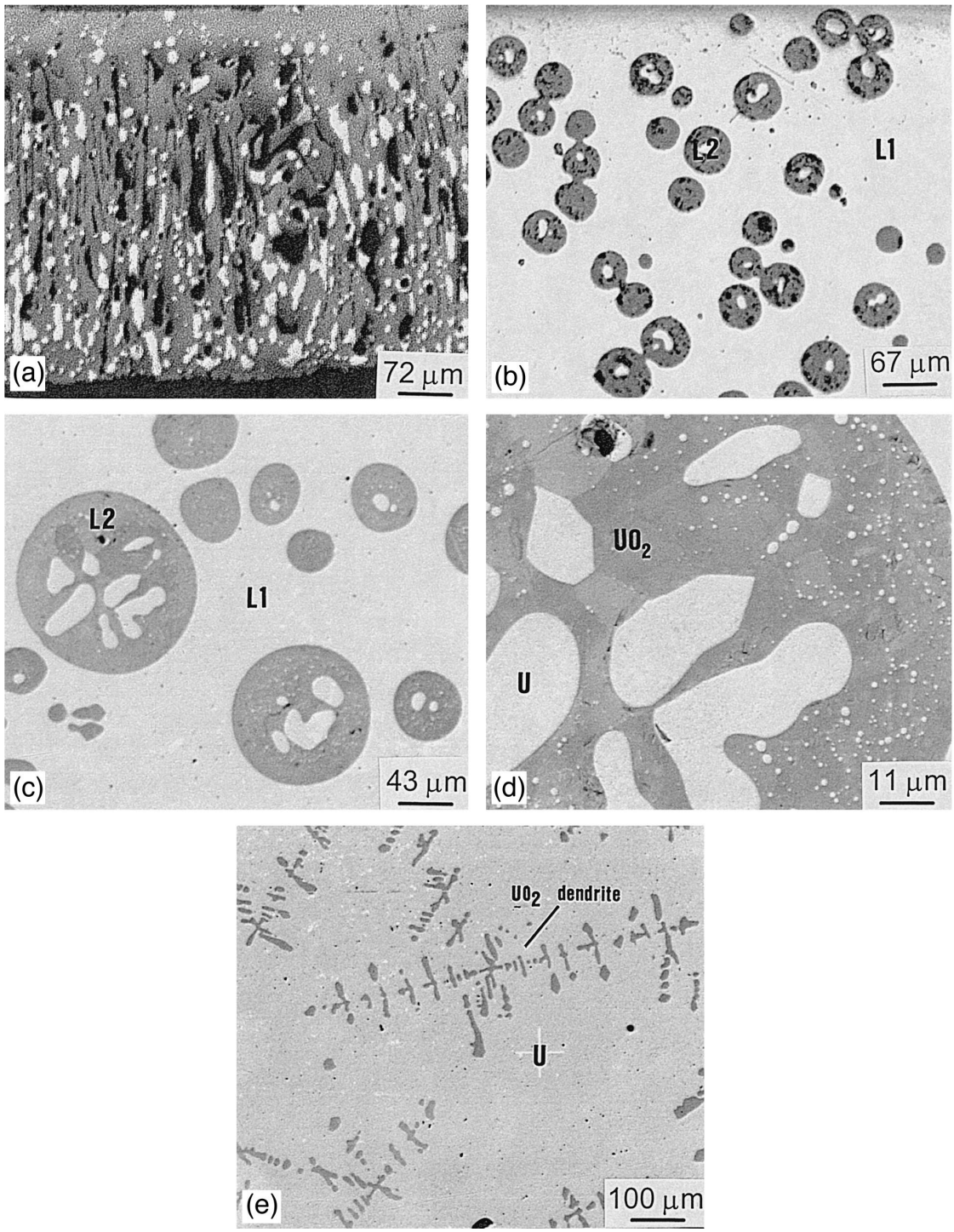

Fig. 8. (a) Electron micrograph showing the surface layer which may correspond to the L2 oxide-rich liquid in the U–UO_2 ingot. (b) Macroscopic view of the section under the surface layer showing the presence of droplets of the L2 oxide minor liquid phase in the L1 parent liquid enriched in uranium. (c) Electron micrograph presenting the droplets of the L2 oxide liquid phase. (d) Electron micrograph showing the quenched structure of the L2 oxide liquid, constituted of a UO_2 matrix and pure uranium area. (e) Electron micrograph showing the microstructure of the L1 uranium rich liquid, constituted of UO_2 dendrites in a pure uranium matrix.

Table 3
Microstructure analysis of the U–UO_2 ingot

	Phase	Phase surf. % by image analysis	Liquid overall composition at 3090 K (at.%)
Uranium-rich liquid L1	UO_2 dendrites	8 ± 2	8 ± 2 O, 92 ± 2 U
	U matrix	92 ± 3	
Oxygen-rich liquid L2	UO_2	77 ± 3	55 ± 2 O, 45 ± 2 U
	U matrix	23 ± 3	

and grow in the liquid (Fig. 8e). The remaining liquid is pure uranium. The overall compositions of both liquid phases L1 and L2 are given in Table 3. The largest droplets located near the surface are analyzed by image analysis assuming that the specimen section cuts in their center and that the microstructure is isotropic. The smaller droplets contain a lower U fraction because the cutting section may be far from their centers. Results are in agreement with the data of Edwards and Martin [2] for the monotectic reaction (Fig. 1). On the other hand, it is inconsistent with the higher O solubility limit data of the other authors [6,11,12].

4.3. O–U–Zr system

The macroscopic aspect of the ingot is described in relation to the position in or out of the miscibility gap. Next, the extrapolation of these experimental results with Thermo-Calc is presented to discuss the consistency of the different results. Finally, the microstructure and the solidification path of the different melts calculated with the Thermo-Calc software are given.

The initial ingot composition and the final melt composition are reported in Fig. 9. The results of the microstructure analysis for all mixtures are given in Table 4.

4.3.1. [UO_2 + Zr] mixtures

4.3.1.1. UO_2–Zr (1). The mixture of UO_2 and Zr is prepared to obtain an overall composition of 49.66 mol UO_2, which may be situated in the miscibility gap as mentioned by Juenke and White [13] (Fig. 2). The relatively low thickness of the melt zone (4 mm) indicates that both temperature and heat flow are not high enough to melt the whole mixture. The final overall composition of the melt is shifted to the zirconium-rich corner in comparison with the initial composition (Fig. 9). This is mainly due to the fact that some UO_2 cylinders have not melted. No droplet or layer is observed. The homogeneity of the microstructure of the melt zone indicates that the final alloy composition is not situated inside the liquid miscibility gap because of the composition shift. This first experiment gives information on the extent of the miscibility gap.

4.3.1.2. UO2–Zr (2). The increase of the power density leads to a larger thickness of the melt of 13 mm. A macroscopic view of an ingot section is shown in Fig. 10a. Below a homogeneous melt zone, some UO_2 bulk pieces are still present. As observed in the previous test, the two areas are separated by a clear interface which may correspond to the liquidus curve. The area below the interface may correspond to a mushy zone. The homogeneity of the quenched melt structure clearly indicates the presence of a single liquid phase (Fig. 10b and c). The alloy composition moved during the experiment to the Zr corner (Fig. 9). This movement is related to the evaporation of the two major species in vapor UO and U [11]. The shift of the alloy composition in comparison with that desired can explain why the miscibility gap could not be observed in the sample. It gives a second point for the determination of the miscibility gap extent in the ternary system.

These two first tests show that the power density was not high enough to melt the whole ingot and also that the ingot overall composition largely changed during the experiment mainly due to the UO and U evaporation and to the UO_2 quantity which had not melted. This suggests working with a thinner ingot and a greater power density. On the other hand, the microstructure analysis between top and bottom of the melt zone indicates that the melt composition is homogeneous. It shows that the experimental conditions do not involve a very high temperature gradient inside the melt zone.

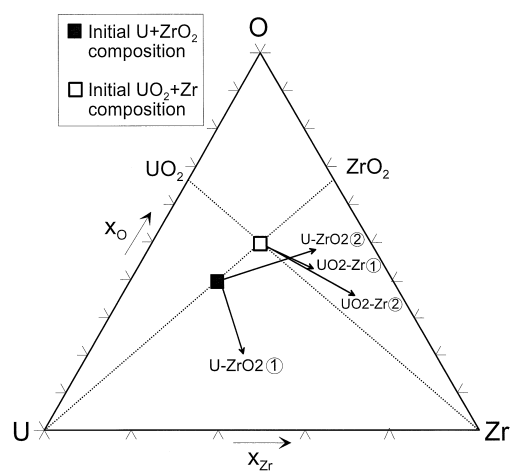

Fig. 9. O–U–Zr section giving the variation of the different melt compositions during the experiment. The initial compositions are reported on the UO_2–Zr and U–ZrO_2 lines.

Table 4
Microstructure analysis and calculated solidification path of the (U,Zr,O) alloys

Alloy designation	UO_2–Zr (1)			UO_2–Zr (2)			U–ZrO_2 (1) Liquid 1			U–ZrO_2 (1) Liquid 2			U–ZrO_2 (2)		
	O at.%	U at.%	Zr at.%	O at.%	U at.%	Zr at.%	O at.%	U at.%	Zr at.%	O at.%	U at.%	Zr at.%	O at.%	U at.%	Zr at.%
Experimental															
Liquid composition	42±4	15±2	43±2	35±4	11±2	54±2	16±4	44±2	40±2	48±4	29±2	23±2	48±4	11±2	41±2
Phase composition (at.%)															
$(U,Zr)O_{2-x}$	65±1	32±1	3±1	–			–	–	–	64±1	33±1	3±1	–		
α-Zr(O)	33±2	2±1	65±2	–			24±2	3±1	73±2	25±2	2±1	73±2	–		
U rich	16±5	81±5	3±1	–			9±5	83±4	8±1	22±5	76±3	2±1	–		
Phase fraction (surf. %)															
$(U,Zr)O_{2-x}$	–			29±3			–			73±3			70±3		
α-Zr(O)	–			70±3			–			23±3			30±3		
U rich	–			1±1			–			4±2			–		
Solidification path calculation (lever rule)															
T liquidus (K) $L \rightarrow L + (U,Zr)O_{2-x}$	2578			2376			2578			2568			2611		
mol% of primary $(U,Zr)O_{2-x}$	45			10			13			68			56		
T solidus (K)	1600			1600			1600			1600			2080		
Phase fraction at T solidus	mol%	vol%		mol%	vol%		mol%	vol%		mol%	vol%		mol%	vol%	
$(U,Zr)O_{2-x}$	39	53		22	33		12	20.5		61	78		52	65	
α-Zr(O)	59	45.5		76	65.5		30	29		28	20.5		48	35	
(γ-U,β-Zr)	2	1.5		2	1.5		58	50.5		11	1.5		0	0	

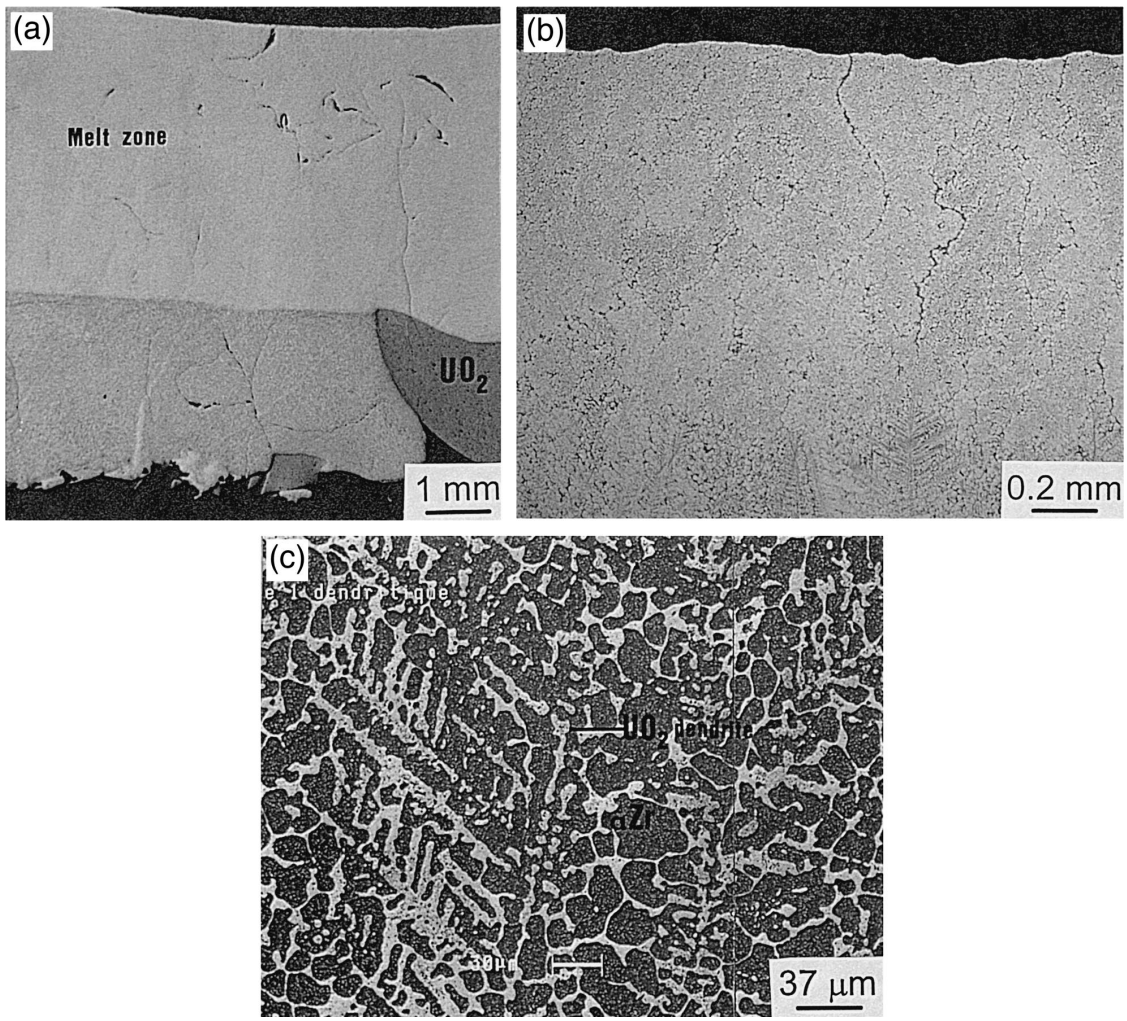

Fig. 10. (a) Macroscopic view of a section of the Zr–UO_2 (2) ingot showing the melt zone. An unmelted UO_2 cylinder is present in the ingot bottom. A clear interface separates the upper melt zone and a mushy zone. (b) Micrograph presenting the homogeneous structure of the quenched liquid phase for the Zr–UO_2 (2). (c) Electron micrograph showing the microstructure of the quenched liquid phase which consists of UO_2 dendrites surrounded by the α-Zr(O) phase.

4.3.2. [U + ZrO_2] mixtures

4.3.2.1. U–ZrO_2 (1). The melt temperature is estimated to be 3223 ± 100 K. The first observation of an ingot cross-section shows that the ingot is wholly melted (Fig. 11a). The presence of spherical droplets with a 150 μm diameter can be noted (Fig. 11b–d). The first optical microscope observation shows that the droplets are constituted of several phases, with a major fraction of oxide when the matrix is U enriched. For the same reasons reported for the U–UO_2 test, there is no doubt that the droplets correspond to the minor oxide liquid phase L2. The overall composition of the melt as well as those of the two liquid phases L1 and L2, measured by several methods, are reported in Fig. 13d. The analysis of the two liquids composition gives a tie-line inside the miscibility gap at 3223 K. The overall composition of the melt is close to the uranium-rich liquid phase L1. This is consistent with the fact that the oxide liquid phase fraction is low. The composition analysis of the droplets has been performed in different points of the ingot. It shows that there is no appreciable change of the droplet composition with its location in the ingot. The structure of the two liquids is very different from that the one observed in the U–Cu system (Fig. 7a), for which the gravity-dependent effects seem to play a dominant role. The main reason may be the altogether higher temperature level in the present experiment which leads to an increase in convection. It can also be due to a lower density difference between the two liquids. The temperature gradient in the ingot can induce a motion of the droplets known

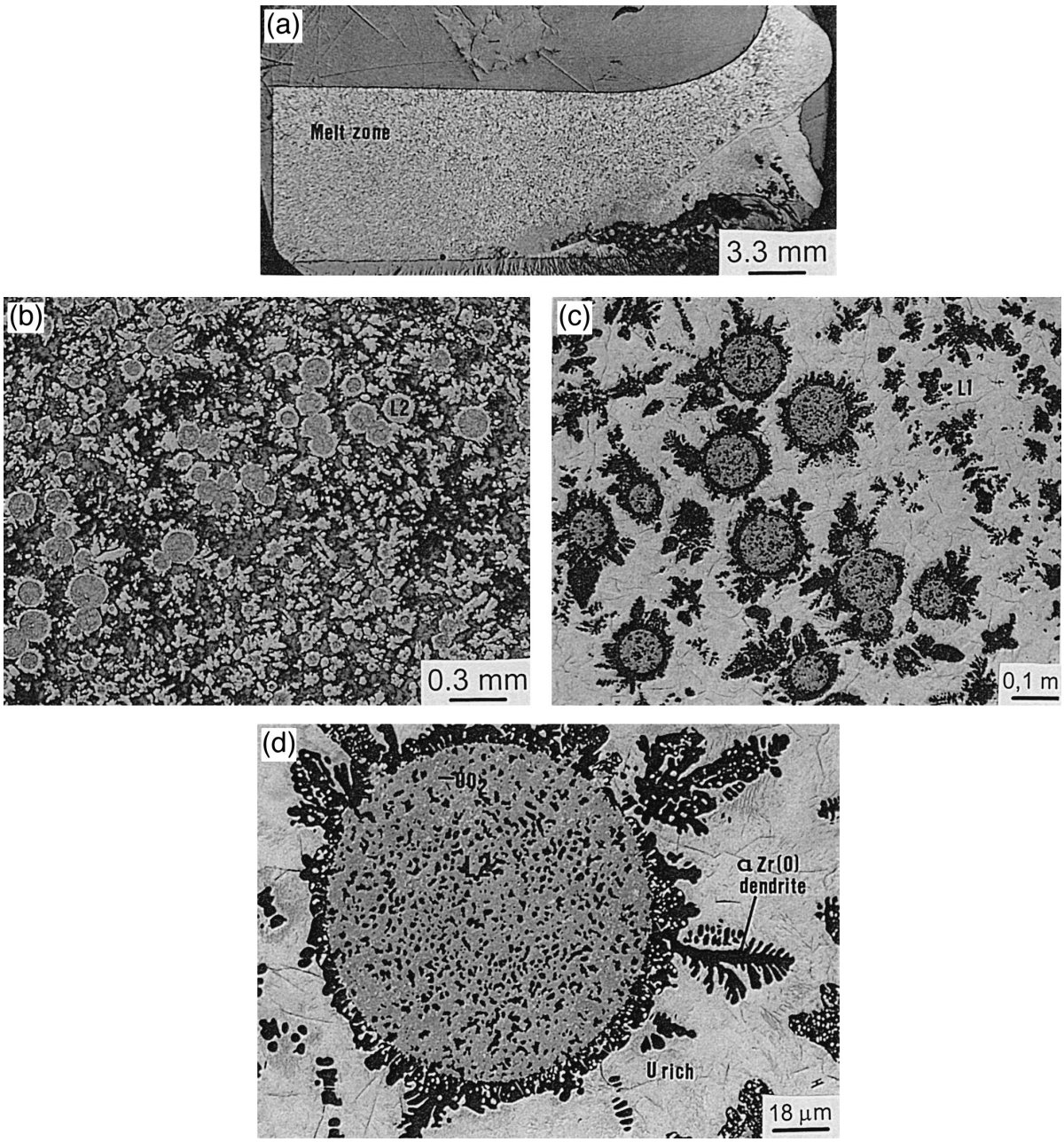

Fig. 11. (a) Macroscopic view of the U–ZrO_2 (1) ingot section, showing that the ingot wholly melted. (b) Micrograph showing the droplets of the L2 minor oxide liquid, which were quenched during their rising to the surface. (c) Electron micrograph showing the α-Zr(O) dendrites (grey) in the uranium-rich matrix (white) of the L1 metallic-quenched liquid. (d) Electron micrograph showing the microstructure of the L2 quenched oxide liquid. It is mainly constituted of the UO_2 phase (grey), small precipitates of α-Zr(O) (black) and very small areas enriched in uranium (white).

as Marangoni [25]. Furthermore, it seems that the oxide liquid is moved from the center to the crucible walls. As the crucible is water-cooled, this leads to the precipitation of the oxide on the walls. It can induce the spread of the liquid to the melt and then, lead to other convective flows within the parent phase. All these convective motions, which, in part, carry the droplets with them, will induce coalescence and coagulation, i.e., collision of droplets and formation of a new droplets, as can be observed (Fig. 11b). It is probably the reason why the droplets are larger near the melt surface as in the bottom of the ingot.

The results of this experiment show that the miscibility

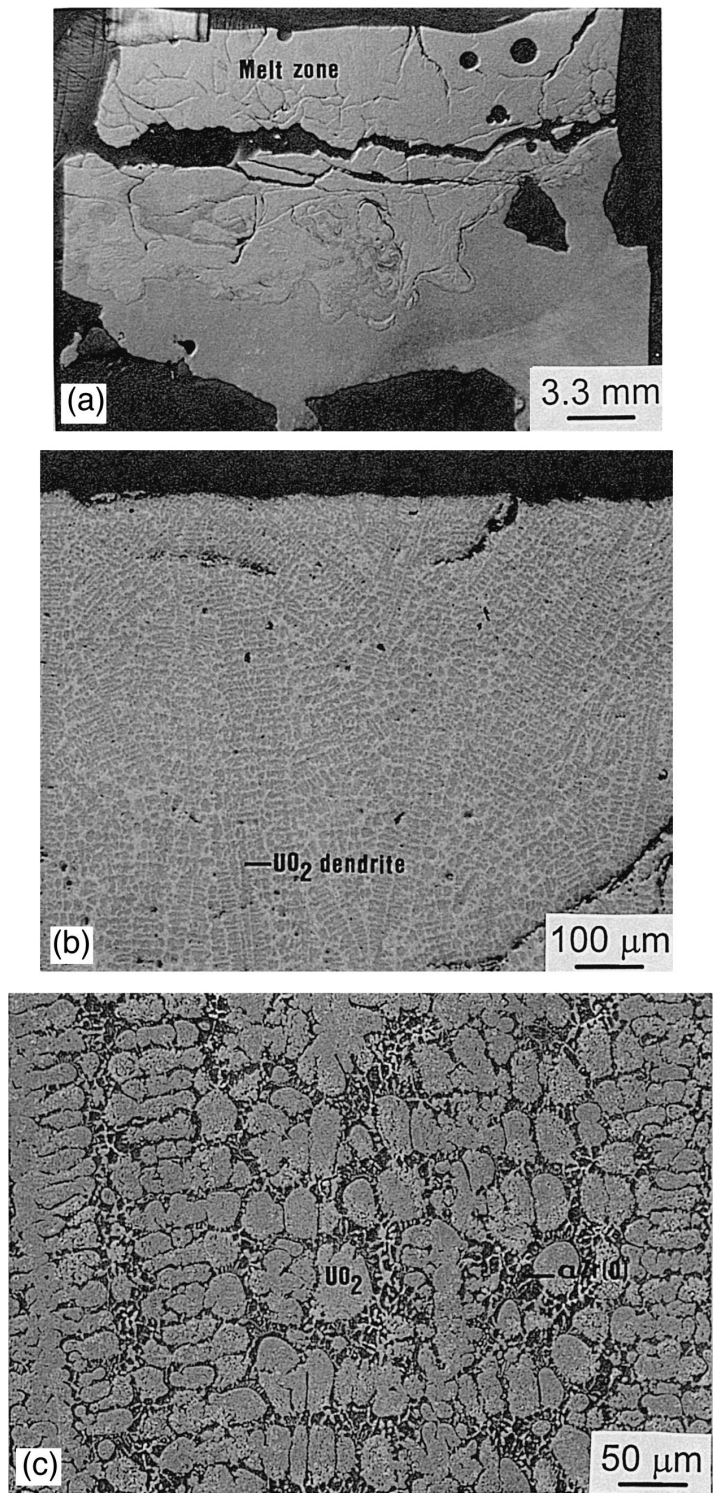

Fig. 12. (a) Macroscopic view of the U–ZrO_2 (2) ingot. The upper part of the ingot is enriched in ZrO_2 while the bottom is uranium-rich. (b) Micrograph showing the homogeneous structure of the quenched liquid phase. (c) Electron micrograph presenting the microstructure of the quenched liquid, mainly constituted of UO_2 dendrites surrounded by the α-Zr(O) phase.

gap extent in the ternary is important. This is in agreement with the large size of the miscibility gap in the U–UO_2 system.

4.3.2.2. U–ZrO_2 (2). In this test, the scanned surface by the electron beam is increased to reduce the evaporation of the elements. The temperature of the melt surface is then significantly decreased to 2900 K. Because the ZrO_2 pieces were placed in the upper part of the ingot at the beginning of the experiment, the melt is enriched in oxide (Fig. 12a–c). The oxide-rich melt is homogeneous and corresponds to a single liquid phase close to ZrO_2 (Fig. 9).

The U–ZrO_2 (3) test reproduces the same results as the U–ZrO_2 (1) ingot.

5. Miscibility gap extent calculation

Thermodynamic calculations are very useful to discuss the consistency between the different experimental data. All the present experimental data as well as some results of the literature have been used to optimize the thermodynamic parameters of the polynomial description of the

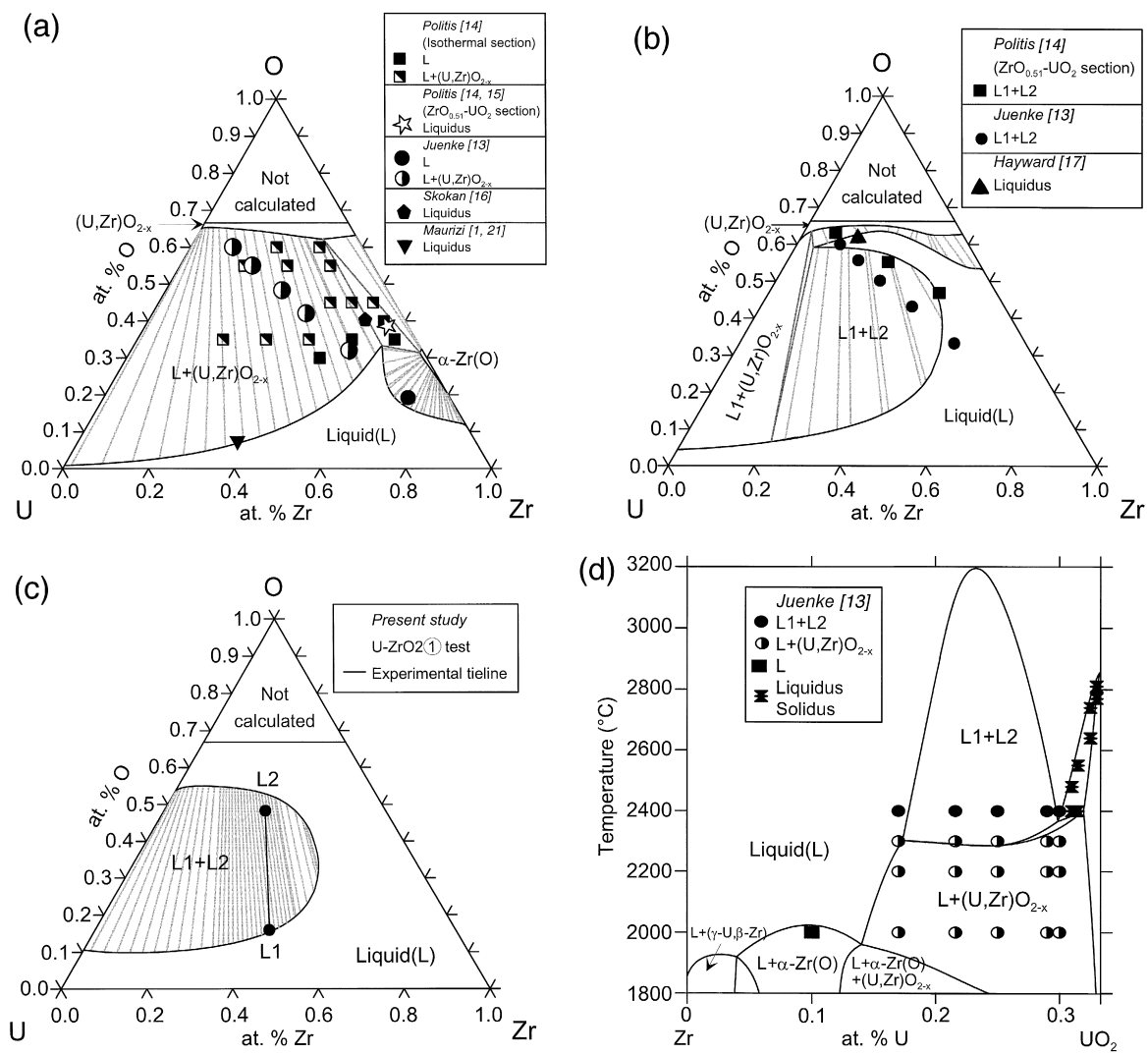

Fig. 13. (a) O–U–Zr isothermal section calculated at 2273 K where the different experimental points are reported. (b) O–U–Zr isothermal section calculated at 2723 K where the experimental results are reported. (c) O–U–Zr isothermal section calculated at 3223 K where the experimental tie-line determined in the present study is reported. (d) Calculated Zr–UO_2 vertical section where the experimental points of Juenke and White [13] are reported.

(O,U,Zr) ternary liquid phase. The O–U–Zr isothermal sections calculated at 2273 K, 2723 K and 3223 K are given in Fig. 13a–c, respectively. The UO_2–Zr section was also calculated and compared to that determined experimentally by Juenke and White [13] (Fig. 13d). Our experimental results are consistent with the lower values of O solubility limit in the liquid (O,U,Zr) of Maurizi [1] and Maurizi et al. [21] and Politis [14] (of the α-Zr(O)–UO_2 section). On the other hand, the calculated liquidus curve at 2273 K shows a significant deviation with the liquidus data of the isothermal section of Politis [14] and at 2273 K close to the UO_2–Zr line (Fig. 13a) [15]. A good agreement is obtained with the miscibility gap extent of Juenke and White [13] and Politis [14] and Hofmann et al. [15]. But our results are inconsistent with the α-Zr(O)–UO_2 section of Hayward and George [17]. The reason why Hayward and George [17] have not observed the miscibility gap could be due to a too low cooling rate of the specimen. Furthermore, the investigated section is located at the limit of the miscibility gap (see Fig. 13b). So if there is a slight change in the melt composition during the experiment, the final composition can be located outside the miscibility gap.

6. Interpretation of the microstructure using solidification path calculation of the (O,U,Zr) liquid phases

Table 4 summarizes the results of the microstructure analysis as well as the solidification path calculation for all the liquid phases entering or not the miscibility gap.

The microstructures of the Zr–UO_2 (2), U–ZrO_2 (1) and U–ZrO_2 (2) mixtures are shown, respectively, in Fig. 10c, Fig. 11c and Fig. 12c. Three phases were identified: (i) the $(U,Zr)O_{2-x}$ mixed oxide with a FCC_C1 structure, containing less than 3 at.% Zr, (ii) the α-Zr(O) interstitial solution of oxygen in the HCP_A3 zirconium with about 30 at.% O and a U solubility of about 2 at.% (in agreement with the results of Yamanaka et al. [19]), (iii) a uranium-enriched zone, probably made up of two phases, whose structure is too thin to characterize the two constituents. The compositions inside these areas are not constant. Their oxygen concentrations vary, partly due to the oxidation of uranium.

The above reported phases are found in all the melt but with different relative fractions as a function of the overall composition. To better understand the solidification sequences during cooling, it is useful to look at the calculated liquidus surface, presented in Fig. 14, where all the overall melt compositions are reported.

It can be noted that all the alloys are situated in the part of the diagram where the $(U,Zr)O_{2-x}$ mixed oxide is the first solid phase which precipitates.

The calculation with Thermo-Calc gives the following reactions.

(i) Close to the liquidus temperature, primary oxide

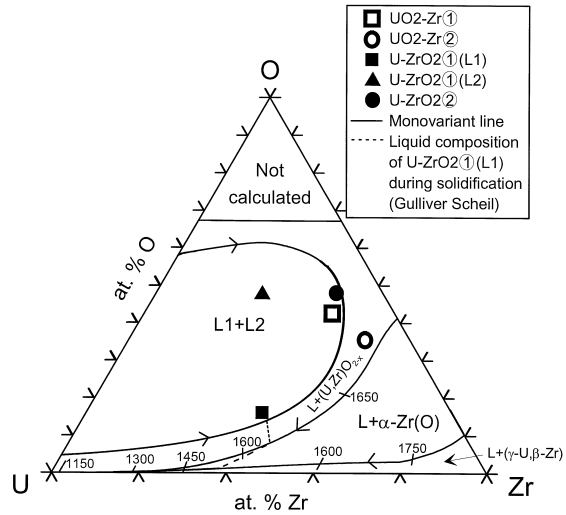

Fig. 14. Liquidus projection of the O–U–Zr system. The plain lines correspond to the monovariant lines. The different liquid compositions are reported. The dashed lines represent the variation of the liquid composition during solidification calculated with the Gulliver–Scheil model for the liquid 1 of the U-ZrO_2 (1) test. It shows that the liquid composition can enter the [Liquid + α-Zr(O)] which could explain the formation of α-Zr(O) dendrite in the liquid 1.

$(U,Zr)O_{2-x}$ precipitates: [Liquid 1 → Liquid 1 + $(U,Zr)O_{2-x}$]. In most of the alloy, the mixed oxide grows in the form of dendrites, except in the droplets of Liquid 2 (U–ZrO_2 (1)), where the oxide fraction is very high (68 mol%).

(ii) When the liquid composition reaches the monovariant line [Liquid 1 + $(U,Zr)O_{2-x}$ + α-Zr(O)], the liquid phase reacts with the mixed oxide during the peritectic reaction: [Liquid 1 + $(U,Zr)O_{2-x}$ → α-Zr(O)]. This peritectic reaction is very slow and is rarely completed because it involves diffusion of the elements through the α-Zr(O) phase. It tends to produce a microstructure which consists of primary $(U,Zr)O_{2-x}$ dendrites with a surface layer of α-Zr(O) [26]. This microstructure is clearly observed in Zr–UO_2 (2) (Fig. 10c) and U–ZrO_2 (2) (Fig. 12c). For the U–ZrO_2 (1) alloy which contains the two liquid phases, the interpretation of the microstructure is more complex. In fact, in liquid 1, the α-Zr(O) phase has two different morphologies. It is found in the form of a band surrounding the droplet of Liquid 2 in Liquid 1 (Fig. 11d), which may correspond to a nonequilibrium interfacial reaction between the $(U,Zr)O_{2-x}$ oxide of Liquid 2 and Liquid 1. As the microstructure of the quenched droplet of Liquid 2 is homogeneous, it can be assumed that this interfacial reaction does not affect the overall composition measurement of Liquid 2. The α-Zr(O) phase can also be observed in the form of dendrites which seem to preferentially germinate on the $(U,Zr)O_{2-x}$ oxide precipitates (Fig. 11d). The form of dendrite cannot result from

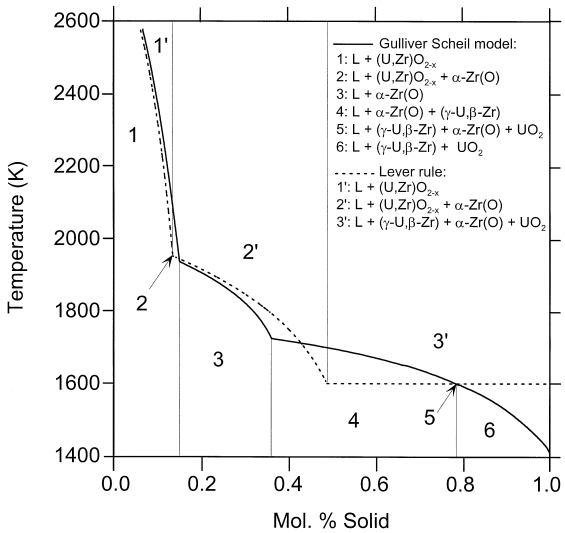

Fig. 15. Variation of the temperature vs. the solid mole fraction during the solidification of the liquid 1 (U-ZrO_2 (1) test). The calculation was performed with two models: the Gulliver–Scheil one (plain line) and the lever rule (dashed line). It gives the different crossed domains during solidification.

the peritectic reaction. It corresponds to the growing of a crystal in a liquid phase. This reaction cannot be predicted by the present equilibrium calculation which is performed only by applying the lever rule in the phase diagram. Moreover, the fast cooling rate of the ingot corresponds to nonequilibrium conditions. The Gulliver–Scheil model [27] was used to calculate the alloy solidification path. In this model, it is assumed that there is no diffusion in the solid state and that the liquid has an homogeneous composition. It leads to the deposition of solid layers with different compositions. In comparison with a solidification path calculated with the lever rule, the liquid composition can follow an other path which can lead to a different phase transformation. Fig. 15 presents the solid mole fraction evolution in the liquid 1 (U–ZrO_2 (1)) alloy vs. temperature during cooling for the two models. In the Gulliver–Scheil model, the liquid composition can cross the [Liquid + α-Zr(O)] domain where dendrites can be formed. It can also be seen in Fig. 14 where the liquid composition can leave the monovariant line [Liquid 1 + $(U,Zr)O_{2-x}$ + α-Zr(O)] to enter the [Liquid + α-Zr(O)] domain.

(iii) Except for the U–ZrO_2 (2) alloy, the remaining fraction of liquid solidifies during an invariant quasi-peritectic reaction [Liquid 1 + α-Zr(O) → (β-Zr,γ-U) + UO_2]. It can be assumed that the U-enriched zone, observed experimentally, corresponds to a [(β-Zr,γ-U) + UO_2] two phase region. The fraction of the remaining liquid is very low, a few percent for all alloys except for the Liquid 1 (U–ZrO_2 (1) sample), where the uranium-rich zone constitutes the matrix. During the reaction, the liquid is almost wholly transformed in (β-Zr,γ-U) solid solution.

The surface fraction of the phase have been measured by image analysis in three alloys and compared to the calculated value with Thermo-Calc (Table 4). It shows an overall correct agreement. The difference can be due to several reasons: (i) the comparison of surface and volume fractions, (ii) the incomplete peritectic reaction which leads to a lower experimental α-Zr(O) fraction, (iii) the non-equilibrium reaction which can be described by the Gulliver–Scheil model.

7. Conclusion

Heating by electron bombardment is a good method to melt and quench materials at very high temperature. The miscibility gap is displayed in the liquid state in the O–U and O–U–Zr systems. The microstructure analysis of the quenched liquid phases allows determination of a tie-line in the O–U miscibility gap at 3090 K as well as in the O–U–Zr ternary system at 3223 K. It shows that the miscibility gap has a large extent in both systems. These experimental data have been used to calculate the O–U–Zr phase diagram with Thermo-Calc. A good agreement is found between the present experimental work and the results of Edwards and Martin [2] in U–UO_2 as well as those of Juenke and White, and Politis, respectively, in the UO_2–Zr and UO_2–α-Zr(O) sub-systems. On the other hand, the results are in contradiction with the data of Hayward and George. The alloy microstructure has been interpreted with the help of solidification path calculation in equilibrium and nonequilibrium conditions. The two liquids have different compositions, one close to U–Zr and the other one, oxygen-rich. The closer the alloy composition is to the U–O system, the larger are the differences in the compositions of the two liquids. The preparation of the alloy by electron bombardment leads to a droplet structure of the minor oxide liquid in the parent metallic liquid phase. The droplets seem to segregate at the ingot surface. This leads to a layer formation in case of the U–O system where there is the greatest difference between the two liquid compositions.

Acknowledgements

We acknowledge the assistance of C. Maillault and J.P. Lang in performing the electron bombardment experiments. The authors express also sincere thanks to S. Goldstein, G. Bordier, D. Camel, K. Froment and J.M. Seiler for their assistance during the study.

Appendix A. Evaporation model

The source flux F_S is deduced from the evaporation area A_S and the measured mean source flow D_S. D_S is

obtained by weighing the ingot before and after the evaporation time. The temperature of the melt is then obtained from the calculated curve $F_S = f(T)$.

The vapour flux F_S is the sum of the flux of the U [11], UO, UO_2, UO_3, Zr, ZrO, ZrO_2 [23] (V. Dauvois, private communication) species calculated by considering a Langmuir flux:

$$F_S(T) = \sum_{i=1}^{N} \sqrt{\frac{M_i}{2\pi RT}}\, p_i(T). \quad (1)$$

M_i and p_i are the molar mass and the partial pressure of the specie i.

The partial pressures p_i are determined from the reactions of formation of the gaseous species from the elements in the melt [11,23] (V. Dauvois, private communication):

$$\log p_U = \log a_U + 5.92 - \frac{26\,210}{T}$$

(from Ref. [11]),

$$\log p_{UO} = \log a_U + \log a_O + 3 + \frac{1376}{T},$$

$$\log p_{UO_2} = \log a_U + 2\log a_O - 0.442 + \frac{25\,498}{T},$$

$$\log p_{UO_3} = \log a_U + 3\log a_O - 4.186 + \frac{45\,360}{T}$$

(from Ref. [23] and V. Dauvois, private communication),

$$\log p_{Zr} = \log a_{Zr} + 6.410 - \frac{30\,711}{T},$$

$$\log p_{ZrO} = \log a_{Zr} + \log a_O + 3.633 - \frac{2682}{T},$$

$$\log p_{ZrO_2} = \log a_{Zr} + 2\log a_O - 0.189 + \frac{17\,343}{T}$$

(from Ref. [23]).

Finally, to determine the temperature, the problem is to estimate the activities of O, U and Zr in the melt. This can be solved by performing several iterations of calculation.

For the U–UO_2 test, the initial temperature of 2980 K is calculated by considering that $a_U = 1$ and $a_O = a_O$[U–UO_2] where the O activity is calculated from the enthalpy of formation of the UO_2 dioxide. In the next step, the activities of O and U are calculated with Thermo-Calc with the fitted temperature corresponding to the previous iteration. A new value of the temperature can then be deduced with the model. Three runs are enough to determine the melt temperature of 3090 ± 100 K for the U–UO_2 test.

For the U–ZrO_2 (1) test, the initial temperature is calculated by assuming that: $a_U = a_{Zr} = x_U = x_{Zr} = 0.5$ and $a_O = a$[U–UO_2] = a[Zr–ZrO_2]. By the same method of calculation, the melt temperature is estimated to be 3223 ± 100 K.

References

[1] A. Maurizi, PhD thesis, Université Pierre et Marie Curie, Paris VI, 1996.
[2] R.K. Edwards, A.E. Martin, Thermodynamics 2 (1966) 423 (IAEA, Vienna).
[3] B. Jansson, PhD thesis, Royal Institute of Technology, Stockholm (1984).
[4] B. Sundman, B. Jansson, J.O. Andersson, Calphad 2 (9) (1985) 153.
[5] C. Guéneau, V. Dauvois, A. Maurizi, to be submitted to J. Nucl. Mater.
[6] P. Guinet, H. Vaugoyeau, P. Blum, French Atomic Energy Commission, Report CEA R 3060, (1966).
[7] M.J. Bannister, J. Nucl. Mater. 24 (1967) 340.
[8] J.L. Bates, Thermodynamics 2 (1966) 73 (IAEA, Vienna).
[9] R.E. Fryxell, D.E. Joyce, R. Szwarc, J. Mater. 25 (1968) 97.
[10] R.E. Latta, R.E. Fryxell, J. Nucl. Mater. 35 (1970) 195.
[11] A. Pattoret, PhD thesis, Université Libre de Bruxelles (1969).
[12] S.P. Garg, R.J. Ackermann, J. Nucl. Mater. 88 (1980) 309.
[13] E.F. Juenke. J.F. White, Report GEMP-731 (1969).
[14] C. Politis, Report KfK 2167 (1975).
[15] P. Hofmann, S. Hagen, G. Schanz, A. Skokan, KfK 4485.
[16] A. Skokan, 5th Int. Meeting on Thermal Nuclear Reactor Safety, Karlsruhe, Sept. 9–13, 1984, pp. 1035–1042.
[17] P.J. Hayward, I.M. George, J. Nucl. Mater. 232 (1996) 13.
[18] H.A. Saller, F.A. Rough, J.M. Fackelman, A.A. Bauer, J.R. Doig, U.S. Atomic Energy Com. Rept. BMI 1023, Columbus, OH (1955).
[19] S. Yamanaka, M. Katsura, S. Imoto, M. Miyake, Inorg. Chim. Acta 140 (1987) 127.
[20] M. Miyake, M. Katsura, S. Yamanaka, J. Nucl. Mater. 154 (1988) 123.
[21] A. Maurizi, C. Guéneau, P. Pérodeaud, B. Schneider, O. Dugne, F. Valin, G. Bordier, EUROMAT 96 Proceedings, Conference on Materials and Nuclear Power, 21–23 Oct. 1996, Bournemouth, UK, pp. 49–56.
[22] C. Guéneau, A. Maurizi, P. Pérodeaud, B. Schneider, O. Dugne, F. Valin, G. Bordier, Revue de Métallurgie, Journées d'Automne 96, 15–17 Oct. 1996, Paris, p. 3.7.
[23] L.B. Pankratz, Thermodynamic Properties of elements and oxides, United States Department of Interior, Bureau of Mines, 1982.
[24] P. Chiotti, V.V. Akhachinskij, I. Ansara, M.H. Rand, The Chemical Thermodynamics of Actinide Elements and Compounds, Part 5, The Actinide Binary Alloys, IAEA, Vienna, 1981.
[25] L. Ratke, S. Diefenbach, Liquid immiscible alloys, Mater. Sci. Eng. R15 (7–8) (1995) 263.
[26] W. Kurtz, D.J. Fisher, Fundamentals of Solidification, 3rd Ed., TransTech, Aedermannsdorf, 1992.
[27] E. Scheil, Z. Metallkd. 34 (1942) 70.